European Journal of Mechanics - B/Fluids
August 2023, Volume 100, Pages 37-51
https://doi.org/10.1016/j.euromechflu.2023.02.006
https://archimer.ifremer.fr/doc/00824/93567/

Simulation of water entry-exit problems highlighting suction phenomena by coupled Eulerian–Lagrangian approach

Goron Mathieu [1, 3, *], Langrand B. [1, 2], Jacques N. [3], Fourest T. [1], Tassin Alan [4], Robert A. [5], Chauveheid D. [5]

[1] DMAS, ONERA, Lille, F-59014, France
[2] Univ. Polytechnique Hauts-de-France, LAMIH, UMR CNRS 8201, Valenciennes, F-59313, France
[3] ENSTA Bretagne, UMR CNRS 6027, IRDL, Brest CEDEX 09, F-29806, France
[4] Ifremer, RDT, Plouzané, F-29280, France
[5] Altair Engineering France, Antony, 92160, France

* Corresponding author : Mathieu Goron, email address : mathieu.goron@onera.fr

bertrand.langrand@onera.fr ; nicolas.jacques@ensta-bretagne.fr ; thomas.fourest@onera.fr ; alan.tassin@ifemer.fr ; arobert@altair.com ; dchauveheid@altair.com

Abstract :

The present study aims to assess the possibility of describing suction using coupled Eulerian-Lagrangian approach. The water entry and subsequent exit of conical and hemispherical bodies is investigated numerically using the Finite Element simulation software Radioss. The numerical method relies on an explicit numerical scheme. An Eulerian and a Lagrangian formulation are considered for the fluid and the structure, respectively. The fluid–structure interaction is based on an immersed contact interface. Particular attention is given to the evolution of the hydrodynamic (positive and negative) force and wetted surface. The numerical results are compared to experimental results from the literature for different impact conditions (maximum velocity and penetration depth). The influence of several parameters of the numerical model is analysed to assess its robustness and improve the numerical results. The numerical model especially shows a satisfying ability to predict suction forces.

Keywords : numerical simulations, fluid-structure interaction, coupled Eulerian-Lagrangian approach, suction, cone, hemisphere

1. Introduction

Hydrodynamic impact arises when a solid body and a liquid enter into contact due to their relative motion. The study of this phenomenon is motivated by various applications such as hull slamming, spacecraft (capsule) landing in water, aircraft and rotorcraft emergency water landing (ditching) [1, 2]. The hydrodynamic loads arising during water impacts can be among the most severe loads to which the structure can be subjected. Therefore, for some applications, hydrodynamic loads should be considered during the structures' sizing and certification exposed to this kind of event.

The phenomena occurring during a hydrodynamic impact are well known for simple impact conditions, such as the two-dimensional, vertical impact of a rigid body with a simple geometry on a quiescent fluid, neglecting gravity. Analytical approaches, often based on the seminal works of von Karman [3] and Wagner [4], have been developed to analyse the pressure distribution acting on the structure. Numerical methods offer the possibility to study these problems with fewer restrictions on the impact conditions. Ribet et al. [5] studied oblique and high-speed impacts of a sphere, wedge and ellipsoid using Lagrangian and ALE formulations, with comparison to experimental results. Faucher et al. [6] studied the vertical water impact of a cylinder using a CEL approach and an adapted anti-dissipative scheme for unstructured meshes. Their results compared well with the experiments in terms of cylinder deformation.

However, with more complex impact conditions, such as the water entry and subsequent exit of a structure or oblique impacts with a large horizontal velocity, more complex hydrodynamic phenomena may appear. Among these hydrodynamic phenomena we can cite suction forces [7, 8, 9, 10], cavitation [11], ventilation [12], aeration [13] and air cushioning [14]. These hydrodynamic phenomena are difficult to model individually with state-of-the-art analytical or numerical approaches. Piro and Maki [8] numerically predicted the suction force during the two-dimensional water entry and exit of rigid and elastic wedges. They used a Finite Volume Method (FVM) with an ALE formulation and a Volume-Of-Fluid (VOF) method to model the interface between air and water. Tassin et al. [9] obtained similar results for the same case using an analytical 2D approach. Del Buono et al. [15] used a hybrid Boundary Element Method-Finite Element Method (BEM-FEM) to model the same two-dimensional water entry-exit problems. The authors compared their numerical results to analytical and experimental data. They highlighted the influence of gravity on the evolution of the hydrodynamic force, which is particularly strong during the exit phase. Both of these studies are in good agreement with the reference results but had been limited to two-dimensional and simple cases. During an aircraft ditching, the mentioned hydrodynamic phenomena may happen simultaneously and influence each other (see Fig. 1), the structure is three-dimensional and deformable, etc. Modelling these complex hydrodynamic impacts can become challenging for the mentioned analytical and numerical approaches. Therefore, these approaches require further development to increase their robustness and use during design or certification procedures.

The present work focuses on the numerical modelling of suction forces. In a ditching context, suction forces develop because of a depression localised near the rear fuselage, where the first contact with the water occurs, as shown in Fig. 1. This phenomenon occurs due to the high horizontal velocity of the structure at impact and the longitudinal curvature of the fuselage. Recent numerical work showed that suction forces could affect the overall aircraft kinematics during ditching [16, 17]. It is thus crucial to consider this phenomenon when numerically modelling realistic industrial applications such as aircraft ditching.

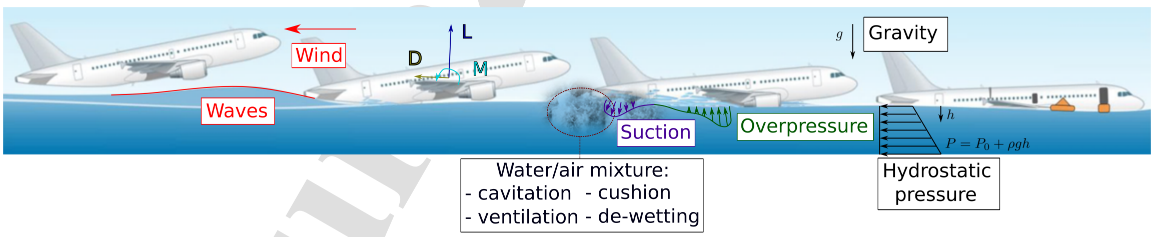

Figure 1: Illustration of the hydrodynamic phenomena occurring during an aircraft ditching.

Advanced numerical approaches are required to study realistic industrial applications such as aircraft ditching. In the literature, the term *advanced numerical approaches* generally refers to high-fidelity and coupled fluid and structure models using, for instance, explicit Finite Elements (FE) solvers. On the one hand, the structure is usually described with a Lagrangian approach. On the other hand, the fluid behaviour can be described using various frameworks: Eulerian, Arbitrary Lagrangian-Eulerian (ALE) [18], or mesh-free methods such as Smoothed Particle Hydrodynamics (SPH) [19, 20]. The coupling between the fluid and structural solutions is a key point because the interdependence between the fluid flow and structural response is important [21, 22].

Advanced numerical approaches have been widely employed to study hydrodynamic impact problems. Stenius et al. [23, 24, 25] studied the hydroelastic response of flat panels during vertical hydrodynamic impact. They used a CEL approach and penalty method to model the fluid-structure interaction. The authors considered different impact velocities, deadrise angles, structural masses and boundary conditions. They highlighted the influence of the structural behaviour on the hydrodynamic response by comparing the structural response and hydrodynamic loading for rigid and hydroelastic cases. N. Toso [16] studied the hydrodynamic impacts of spheres, cylinders, wedges, a NACA body (as reported in [7]) and a full-scale helicopter sub-floor. The author compared the experimental results to the results obtained with a FE method, a SPH method and a combined SPH-FE approach. An overall good agreement between the experiments and the simulations had been found, with more difficulty with modelling the more complex cases, particularly in terms of pressure measures. M.H. Siemann and B. Langrand [26] assessed the ability of SPH and Coupled Eulerian-Lagrangian (CEL) methods to model the oblique impact of aircraft panels undergoing large deformations. Recently, several studies [27, 28, 29, 30] presented simulations of complex water impact problems, such as three-dimensional water entry of bodies with a complex shape and aircraft ditching, based on the SPH method.

From the literature, it appears that several numerical approaches can deal with water impact problems, from simple shapes to more realistic industrial applications. In particular, CEL models are commonly applied to these problems. If their capacity to describe impact forces (high positive pressures) is quite well established through detailed comparisons with experiments, this is not the case when complex hydrodynamic phenomena occur. Studies dedicated to the modelling of three-dimensional hydrodynamic impacts involving suction forces and the related de-wetting process are scarce. In the present work, the ability of the CEL method presented in [26] to model suction is assessed. The issue of the evolution of the wetted surface is also considered.

Different experimental results taken from the literature [31] are used in this work to assess the capacity of the computational method to model (i) suction forces and (ii) the water exit phenomenon. These simple test cases consist of low-velocity water entry and subsequent exit of different structures (cone, hemisphere) at different maximum impact velocities ($U_{max} \in [0.4, 0.6]$ m/s). During the water entry and subsequent exit of the structures, the vertical velocity varies from $-U_{max}$ (the structure enters the water) to U_{max} (the structure exits the water). Suction forces are observed because of this vertical velocity variation, with the maximum deceleration occurring at the end of the entry stage. The numerical results are compared to the experimental results in terms of hydrodynamic force and wetted surface radius. The numerical approach is used to model a "simple" axisymmetric case using a three-dimensional formulation to assess its capacity to model suction loads before modelling more complex test cases closer to an aircraft ditching. Another relevant aspect of these test cases concerns the velocities considered. The order of magnitude of the velocities is close to the ones specified by the airworthiness authorities under aircraft ditching regulations. Indeed, during ditching, the airspeed is set to achieve the minimum rate of descent at touchdown. For example, the certification of the Airbus A320 relies on tests with a descent rate of approximately 1 m/s [32]. In [17], the ditching of a generic rigid aircraft body had been modelled with a structural vertical velocity of 1.5 m/s.

This paper is organised as follows. Section 2 provides a brief presentation of the water entry-exit experiments, a description of the associated numerical model and the analysis methods. The effect of some key numerical parameters on the numerical results is presented in Section 3. Section 4 compares the numerical and experimental results. Finally, conclusions are drawn and orientations for future research are discussed in

Section 5.

2. Water entry and subsequent exit problems and associated computational models

The present work focuses on the water entry and subsequent exit experiments described in [31]. A brief presentation of the experiments is given hereunder. Then follows a description of the fundamentals of the adopted fluid-structure method. Finally, the methods used to obtain the hydrodynamic force and wetted surface radius are presented.

2.1. Description of the experiments

The water entry and subsequent exit experiments have been conducted in a water tank with a 6 Degrees-Of-Freedom (DOF) motion generator [31]. The 6-DOF motion generator enforces the displacement of the mock-up (vertical translation). During the experiments, the vertical velocity varies from $-U_{max}$ (the structure enters the water) to U_{max} (the structure exits the water). The maximum impact velocity reached during the experiments (U_{max}) ranges from 0.4 to 0.6 m/s. The vertical position of the lowest point of the mock-up is defined by the equation $z = h(t)$ and the function $h(t)$ defined as:

$$\begin{cases} h(t) = -H sin(2\pi(t - t^0)/T) + \delta_z, & t^0 \leq t \leq T/2 + t^0 \\ \dot{h}(t) = U_{max}, & t \geq T/2 + t^0 \end{cases} \tag{1}$$

where H is the maximum submergence depth, t^0 is the instant when the structure starts decelerating (see Fig. 7), $T = 2\pi H/U_{max}$ is the period of the structure kinematics, U_{max} is the maximum velocity, and $\delta_z = 3$ mm is a small parameter introduced in [31] a posteriori to compensate for a vertical offset of the mock-up during the experiments. The acceleration is maximum at the transition between the entry and the exit phase (at $t = T/4 + t^0$).

Transparent mock-ups made of polymethyl methacrylate (PMMA) and LED edge-lighting techniques have been used to improve the visualisation of the wetted surface (see Fig. 2 and 3), as described in [33].

2.2. Numerical model

The present hydrodynamic impact problem is modelled using the explicit solver *Radioss*, developed by Altair. The structures and fluid domains are three-dimensional. However, only a quarter of the impact problem is modelled because the problem is axisymmetric. This reduces the size of the model and the associated computation time. Moreover, it was checked that the use of symmetry conditions does not affect the results of the simulations. The computations have been performed using a cluster available at ONERA, whose characteristics are given in Table 1.

Central Processing Unit (CPU) type	Intel(R) Xeon(R) CPU E5-2650 v4
Frequency (GHz)	2.20
RAM (GB)	128
Number of CPUs	64
Computing mode	Distributed memory, double precision

Table 1: Description of ONERA's cluster: hardware and computational settings.

2.2.1. Structure modelling

The dimensions of the mock-ups are given in Fig. 2 and 3 [31]. The structure is discretized using Mindlin-Reissner four-nodes bi-linear shell elements of 15 mm thickness. The characteristic structural element size is 10×10 mm^2. The normal of the structural elements is oriented outward (toward the water). The structure is modelled as a rigid body: the nodes of the structure are kinetically linked to a primary node (see Fig. 4).

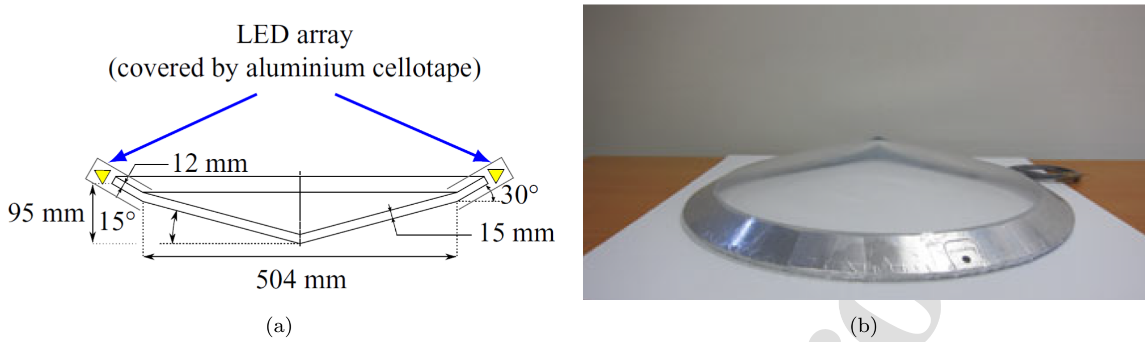

Figure 2: (a) Sketch and (b) photo of the conical mock-up used in the experiments of [31].

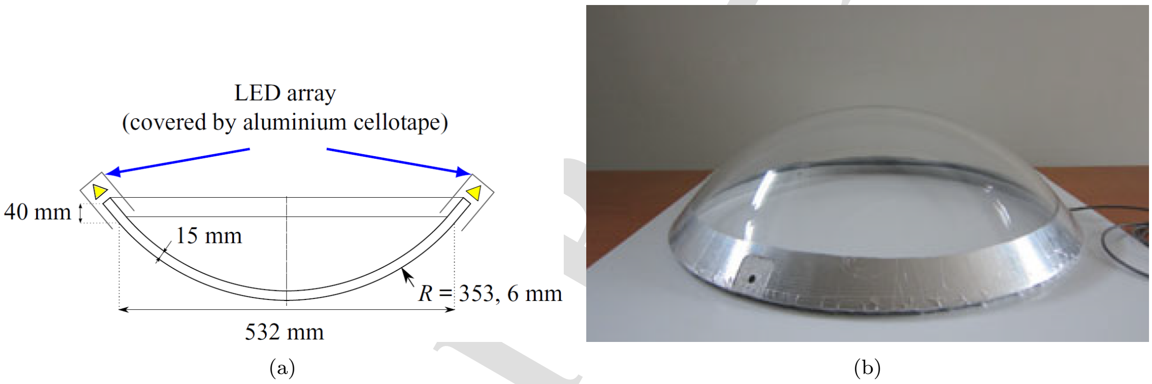

Figure 3: (a) Sketch and (b) photo of the hemispherical mock-up used in the experiments of [31].

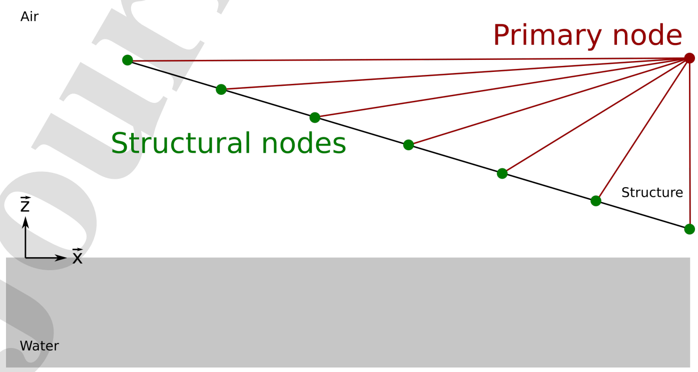

Figure 4: Illustration of the rigid structure model. The kinematic links between the structural nodes (green points •) and the primary node (red point •) are represented by the red lines -.

2.2.2. Fluid modelling

The fluid flow is described by an Eulerian multi-material formulation (*Radioss* law 51). Fluid viscosity and surface tension effects are neglected, and adiabatic conditions are assumed. The validity of these assumptions in the present case is discussed in section 5.1 of reference [31]. Two phases are considered, air and water. The interface between the different phases is a diffuse zone. The fluid mixture is modelled through a so-called six-equation model as described in [34]. The transport equation for the air volume fraction α_a is given by:

$$\frac{\partial \alpha_a}{\partial t} + \vec{V} \cdot \nabla \alpha_a = 0 \tag{2}$$

where $\vec{V}$ is the fluid velocity. The water volume fraction is then obtained by $\alpha_w = 1-\alpha_a$. The evolution of the mass density for each phase is given by Eq. (3) and (4):

$$\frac{\partial(\alpha_a \rho_a)}{\partial t} + \mathrm{div}\left(\alpha_a \rho_a \vec{V}\right) = 0 \tag{3}$$

$$\frac{\partial(\alpha_w \rho_w)}{\partial t} + \mathrm{div}\left(\alpha_w \rho_w \vec{V}\right) = 0 \tag{4}$$

where ρ_a and ρ_w are the air and water mass density, respectively. A single velocity field is used to describe the motion of the different phases:

$$\frac{\partial(\rho \vec{V})}{\partial t} + \mathrm{div}\left(\rho \vec{V} \otimes \vec{V}\right) + \nabla P = 0 \tag{5}$$

where $\rho = \alpha_a \rho_a + \alpha_w \rho_w$ is the mass density of the mixture and P is an equilibrium pressure to be determined later on. The specific internal energies of the air (e_a) and water (e_w) are given by Eq. (6) and (7), respectively:

$$\frac{\partial(\alpha_a \rho_a e_a)}{\partial t} + \mathrm{div}(\alpha_a \rho_a e_a) + \alpha_a P_a \,\mathrm{div}\, \vec{V} = 0 \tag{6}$$

$$\frac{\partial(\alpha_w \rho_w e_w)}{\partial t} + \mathrm{div}(\alpha_w \rho_w e_w) + \alpha_w P_w \,\mathrm{div}\,\vec{V} = 0 \tag{7}$$

where P_a and P_w are the pressure of the air and water, respectively. Eq. (2), (3), (4), (5), (6) and (7) are closed by two equations of state (one for each phase). The air behaviour is modelled using an ideal gas equation of state:

$$P_a = (\gamma_a - 1)\rho_a e_a \tag{8}$$

where γ_a is the heat capacity ratio for air at ambient temperature. The values of the mentioned parameters are synthesised in Table 2. The water behaviour is modelled using a stiffened gas equation of state:

$$P_w = (\gamma_w - 1)\rho_w e_w - \gamma_w P^* \tag{9}$$

where γ_w is the heat capacity ratio for water, P^* is a pressure coefficient ensuring a stable value of the speed of sound in the medium c_s, thus of the water compressibility, regardless of the pressure variation. In practice, Eq. (10) below is used to define P^*. The values of the mentioned parameters are synthesised in Table 3.

$$P^* = \frac{\rho_w^0 c_s^2}{\gamma_w} \tag{10}$$

The equilibrium pressure P used in Eq (5) is computed as follows. The air and water masses are computed for given values of α_a, α_w, ρ_a, ρ_w in an element:

$$\begin{aligned} m_a &= \alpha_a \rho_a, \\ m_w &= \alpha_w \rho_w \end{aligned} \tag{11}$$

Then the values for P, e_a, e_w, ρ_a, ρ_w, described by the system of five equations (Eq. (12)), are computed using a Newton-Raphson iterative method and considering m_a and m_w constant:

$$\begin{cases} \frac{m_a}{\rho_a} + \frac{m_w}{\rho_w} - 1 = 0, \\ e_a - e_a^0 + P \cdot \left(\frac{1}{\rho_a} - \frac{1}{\rho_a^0} \right) = 0, \\ e_w - e_w^0 + P \cdot \left(\frac{1}{\rho_w} - \frac{1}{\rho_w^0} \right) = 0, \\ P_a(\rho_a,\, e_a) = P, \\ P_w(\rho_w,\, e_w) = P \end{cases} \tag{12}$$

The spatial discretization of the momentum balance equation (Eq. (5)) is based on a Lagrange-projection method [34]. The Lagrange step is dealt with using a Monotonic Upstream-Centered Scheme for Conservation Laws (MUSCL). This second-order advection scheme reduces the diffusion problem at the interface between the two phases (*i.e.* air and water). Fluid nodes with an initial vertical position $z_0 \geq 0$ mm are initially located in the air sub-domain. Similarly, fluid nodes with an initial vertical position $z_0 \leq 0$ mm are initially located in the water sub-domain. As mentioned previously, only a quarter of the fluid domain is modelled. Symmetry conditions are applied to the symmetry planes of the model. For the reference mesh, the size of the fluid elements is equal to $2.5 \times 2.5 \times 2.5$ mm^3 near the structure (impact zone). The structure is located within the impact zone at every instant of the computation. The dimensions of the fluid domain are chosen large enough to avoid border effects (*e.g.* reflections of pressure waves) and are given in Fig. 5. The fluid domain is discretized with 8 140 520 3D continuum 8-node elements with one integration point. Other meshes have also been built, and the influence of the size of the fluid elements in the impact zone is discussed in Section 3.3.

In the air domain, the air fraction is initialised to a value $\alpha_{air} = 1$ and the water fraction to $\alpha_{water} = 0$. In the water domain, the air fraction is initialised to a value $\alpha_{air} = \epsilon$ and the water fraction to $\alpha_{water} = 1 - \epsilon$, with $\epsilon = 10^{-4}$. Introducing a small fraction of air into the water guarantees $P > 0$ and $c_s^2 > 0$, thus it guarantees the hyperbolicity of the problem.

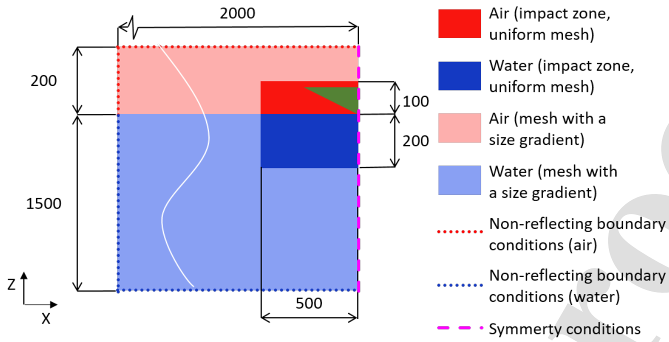

Figure 5: Dimensions and mesh of the fluid domain (in mm). Outside the impact zone, the size of the fluid elements scales with a factor of 1.2. The cone is represented in green.

Parameters	Values
γ_a	1.4
ρ_a^0	$1.22 \cdot 10^{-6}$ g/mm^3
P_a^0	0.101325 MPa

Table 2: Parameters for the air equation of state: ideal gas.

Parameters	Values
γ_w	4.4
ρ_w^0	$1.0 \cdot 10^{-3}$ g/mm^3
P_w^0	0.101325 MPa
c_s	1500 m/s

Table 3: Parameters for the water equation of state: stiffened gas.

2.2.3. Fluid-structure interaction

The fluid-structure interaction is modelled using a "weak" coupling approach [22]. The structural Lagrangian elements (primary elements) are immersed in the Eulerian fluid grid (secondary nodes). The structure and fluid domains are meshed independently and superimposed. The coupling algorithm uses an influence zone defined over a distance h_c in the direction normal to the structure (see Fig. 6). When a fluid node is detected inside the influence zone, a coupling force is applied to it. The coupling force is computed using Eq. (13):

$$F = \frac{k_c}{h_c} d \cdot \tilde{d} \tag{13}$$

where h_c is the contact height, k_c is the contact stiffness, d is the penetration of a fluid node inside the influence zone of the structure and $\tilde{d}$ is the displacement of a fluid node once it is detected inside the influence zone of the structure (see Fig. 6). d and $\tilde{d}$ are computed using Eq. (14) and (15), respectively:

$$d = \max(0, h_c - \mid (\vec{r}_{fluid} - \vec{r}_{lag}) \cdot \vec{n} \mid) \tag{14}$$

where $\vec{r}_{fluid}$ is the position of the projected fluid node on the Lagrangian surface, $\vec{r}_{lag}$ is the position of the Lagrangian node.

$$\begin{cases} \frac{\mathrm{d}\tilde{d}}{\mathrm{d}t} = (\vec{V}_{fluid} - \vec{V}_{lag}) \cdot \vec{n}, & \text{if } d > 0 \\ \frac{\mathrm{d}\tilde{d}}{\mathrm{d}t} = 0, & \text{if } d \leq 0 \end{cases} \tag{15}$$

where $\vec{V}_{fluid}$ is the velocity of the fluid node, $\vec{V}_{lag}$ is the velocity of the structure. The value of the displacement is null at the instant t^i when the fluid node enters the influence zone, *i.e.* $\tilde{d}(t^i) = 0$. The *Radioss* documentation suggests to use the following values for h_c and k_c:

$$h_c = 1.5 \times l_f \tag{16}$$

$$k_c = \frac{\rho_w^0 U_{max}^2 S_{el}}{h_c} \tag{17}$$

where l_f is the size of the fluid elements in contact with the structure, U_{max} is the structure maximum velocity and S_{el} is the mean surface of the structural elements.

This method has been applied to different hydrodynamic impact problems, namely the vertical impact of a wedge [35], the ditching of deformable fuselage sections [26] and the ditching of a helicopter [36].

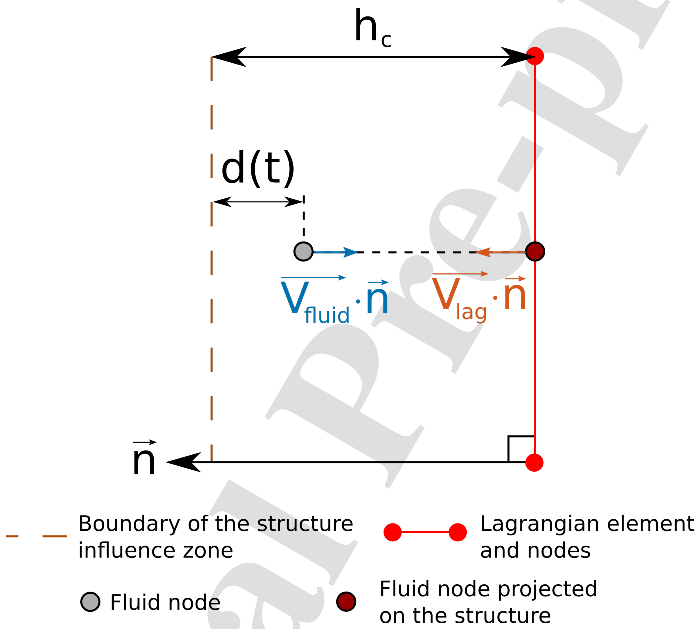

Figure 6: Illustration of the penetration of a fluid node inside the influence zone of the structure, $d(t)$. The relative velocity of the fluid node regarding the Lagrangian (structural) element is $(\vec{V}_{fluid} - \vec{V}_{lag}) \cdot \vec{n}$.

2.2.4. Initial and boundary conditions

It has been observed that the water is pushed down and significant contact forces are observed before the structure reaches the undisturbed water level. This phenomenon is due to the contact algorithm used in the present numerical model (presence of the structure influence zone, see Section 2.2.3). To compensate for this phenomenon, an additional vertical offset equal to h_c is given to the structure in the numerical simulations. Therefore, the bottom boundary of the influence zone of the structure in the simulations is at the same position as the (physical) structure in the experiments (see

Fig. 7). Hence, the motion of the structure in the simulations is prescribed according to Eq. (18), which is obtained by adding the term h_c to Eq. (1):

$$\begin{cases} h(t) = -Hsin(2\pi(t-t^0)/T) + \delta_z + h_c, & t^0 \leq t \leq T/2 + t^0 \\ \dot{h}(t) = U_{max}, & t \geq T/2 + t^0 \end{cases} \tag{18}$$

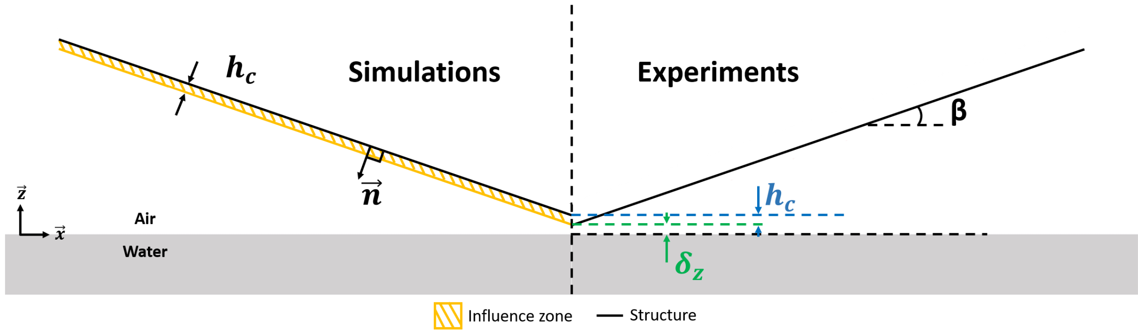

Figure 7: Position of the structure in the numerical simulations (left) and the experiments (right) at t^0, *i.e.* at the time when the structure starts decelerating. h_c is the contact height, δ_z is the parameter introduced a posteriori in the experiments, and β is the deadrise angle of the cone.

Gravity is applied to all the nodes of the model in the $\vec{z}$ direction ($\vec{g} = -9.81\,\vec{z}\,\mathrm{m/s^2}$). Gravity is used to initialise the pressure field in the fluid domain using the following relation:

$$P = P^0 + \rho^0 g z \tag{19}$$

where $P^0 = 0.101325$ MPa is the initial pressure at $z = 0$, g is the gravity acceleration, ρ^0 is the initial fluid mass density and z is the vertical coordinate (recall that $z = 0$ mm corresponds to the initial air-water interface).

At the boundaries of the fluid domain corresponding to symmetry planes, the velocity in the direction normal to the fluid domain is set at zero. Non-reflecting boundary conditions, based on the pressure formulation given in [37], are applied to the other boundaries of the fluid domain.

2.3. Results analysis

For the sake of the numerical approach validation, the numerical results are compared to the experimental ones in terms of non-dimensional hydrodynamic force and wetted surface radius. The non-dimensional hydrodynamic, f_{adim}, force is defined as:

$$f_{adim} = \frac{F_z}{\rho U_{max}^2 S} \tag{20}$$

where F_z is the vertical hydrodynamic force acting on the rigid body due to the fluid-structure coupling algorithm. $S = \pi R^2$ is the projected area of the structure and R is the structure radius.

The relative difference between the experimental and numerical maximum and minimum values of the non-dimensional forces, respectively $\Delta f_{adim\ max}$ and $\Delta f_{adim\ min}$, are defined as:

$$\Delta f_{adim\ max} = \frac{f_{adim\ exp\ max} - f_{adim\ num\ max}}{f_{adim\ exp\ max}} \tag{21a}$$

$$\Delta f_{adim\ min} = \frac{f_{adim\ exp\ min} - f_{adim\ num\ min}}{f_{adim\ exp\ min}} \tag{21b}$$

The wetted surface radius analysis requires a specific post-processing operation of the computational results. For this purpose, the air volume fraction in the fluid elements at a symmetry plane is monitored (see Fig. 8a). Then, the iso-line corresponding to a volume fraction of 0.5 (assumed to correspond to the position of the air-water interface) is extracted from this data. The wetted surface radius is taken as the radial position of the highest point of this iso-line (see Fig. 8b).

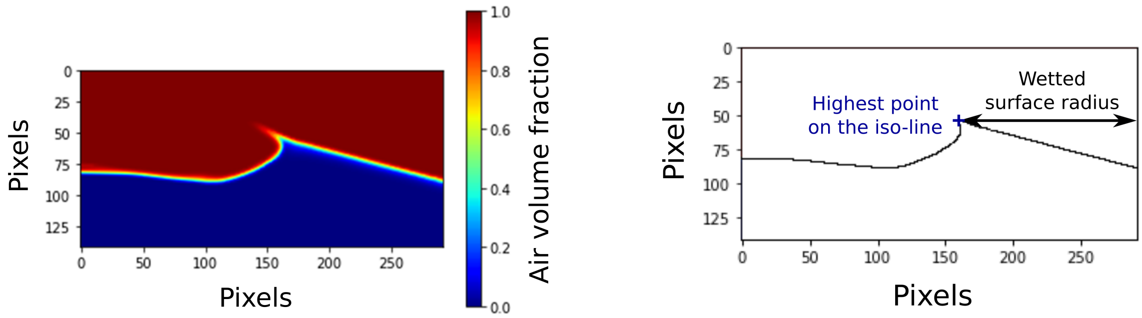

(a) (b)

Figure 8: Water entry and subsequent exit of the cone at $t = 245$ ms. (a) Visualisation of the volume fraction in the fluid elements at a symmetry plane. (b) Extraction of the iso-line corresponding to a volume fraction of 0.5, of the position of the highest point on this iso-line (blue cross $+$) and of the wetted surface radius.

The evolution of the pressure has been monitored numerically at different locations of the structures. The position of the pressure gauges are described for the cone and the hemisphere in Fig 9a and Fig. 9b respectively. Note that the pressure gauges are located outside the influence zone of the structures. Indeed, due to the coupling method used in the present study (penalty method), the pressures obtained inside the influence zone of the structure are noisy and difficult to analyse. Inside the influence zone of the structure, the fluid elements contain an air-water mixture. It means that the volume fraction of the elements in the influence zone rapidly oscillates over time, between $\rho_w^0 = 10^{-3}$ g/mm^3 and $\rho_a^0 = 10^{-6}$ g/mm^3. The oscillations (noise) of the volume fraction induce the oscillations of the pressure results. The numerical results are presented in terms of pressure coefficient, p_{adim} (see Eq. (22)). The numerical pressure results are not compared to experimental results because pressures had not been measured during the experiments.

$$p_{adim} = \frac{P - P^0}{\rho_w^0 U_{max}^2} \qquad (22)$$

where P is the pressure measured by the gauges and P^0 is the initial pressure.

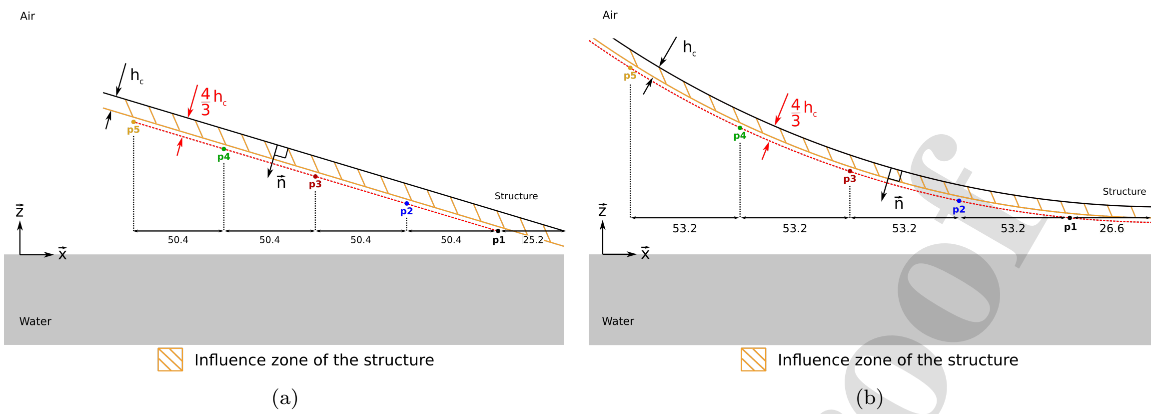

Figure 9: Illustration (not to scale) of the pressure gauges position for (a) the cone and (b) the hemisphere. The distance between the gauges are given in millimetres.

3. Investigation of different numerical parameters affecting the water entry and subsequent exit simulations

The effect of several simulation parameters had been studied in [35] for the water entry of a wedge. This study helped us define guidelines for the simulation of hydrodynamic impacts with the numerical method presented in this paper. It has been noted that the fluid elements near the impacting structure (impact zone) should be at least two times smaller than the structure elements to ensure fluid-structure interaction continuity. The size of the fluid elements outside the impact zone can be increased gradually to reduce the number of fluid elements in the model (a factor of 1.2 between the sizes of two adjacent elements has been found to be suitable). The impact zone dimensions should be equal to twice the structure dimensions. Also, the dimensions of the (entire) fluid domain should be large enough to avoid boundary effects. Following this preliminary work, the influence of different model parameters is studied in this section. The following points are discussed: the effect of the speed of sound in the water, the effect of the contact stiffness (used for the fluid-structure interaction) and the effect of the size of the fluid elements in the impact zone (around the structure). The results are presented for the water entry and subsequent exit of the cone with $c_{max} = 250$ mm (maximum wetted surface radius) and $U_{max} = 0.6$ m/s. The maximum wetted surface radius corresponds to the theoretical value obtained with the Wagner theory when the penetration depth is maximum (see section 2.4 in [31]).

3.1. Effect of the speed of sound in the water

As presented in Section 2.2.2, the water equation of state depends on the speed of sound in the medium (c_s), among other parameters. In explicit simulations, the stable time step depends on the sound celerity. Therefore, it can be beneficial in terms of computation time to use a speed of sound value smaller than the real value for the water (approximately $c_s = 1500$ m/s). Simulations have been performed with different speed of sound values: $c_s = \{200; 500; 1500\}$ m/s (other parameters remaining identical). The results in terms of hydrodynamic force are presented in Fig. 10. The results show that decreasing the value of c_s in the computation leads to a slight reduction of the absolute force value. This maximum value is reached at the transition between the entry and exit stages (note that the force is negative at this time). A decrease of 2.3% and 5.5% is observed for $c_s = 500$ m/s and $c_s = 200$ m/s, respectively, in comparison to the case with $c_s = 1500$ m/s. The computation times are given in Table 4. The computation time needed to complete this simulation with $c_s = 1500$ m/s is more than 3 times higher than with $c_s = 500$ m/s. The loss of accuracy in terms of hydrodynamic peak force predictions ($\simeq 2.3\%$) had been considered reasonable concerning the gain in computation time (3 times less). The results presented in the following paper have been obtained with $c_s = 500$ m/s.

An alternative linear polynomial equation of state has also been tested to describe the water behaviour (see Eq. (23)). The results obtained with both equations of state are very similar (for the same values of c_s). The stiffened gas equation of state (Eq. (9)) is used in the following simulations.

$$P = P^0 + \rho_w c_s^2 \tag{23}$$

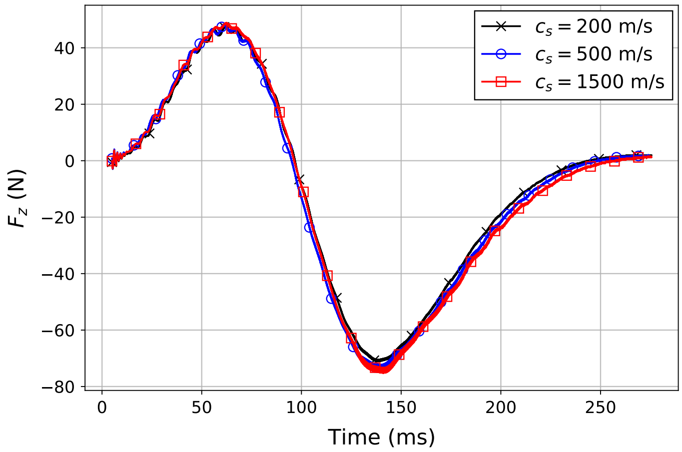

Figure 10: Time history of the hydrodynamic force during the water entry and subsequent exit of the cone, with $c_{max} = 250$ mm and $U_{max} = 0.6$ m/s, for several values of the speed of sound in the water: $c = \{200, 500, 1500\}$ m/s.

c_s (m/s)	200	500	1500
Computation time (DD-hh:mm:ss)	2-08:53:01	3-11:02:05	10-11:27:38

Table 4: Simulation of the water entry and subsequent exit of the cone, with $c_{max} = 250$ mm and $U_{max} = 0.6$ m/s. Comparison of the computation time for $c_s = \{200; 500; 1500\}$ m/s.

3.2. Effect of the contact stiffness

In this section, the effect of the contact stiffness parameter k_c on the hydrodynamic force is analysed. The numerical results obtained for the water entry and subsequent exit of the cone, with a fluid element size of $l_f = 2.5$ mm, are presented in Fig. 11 for different values of k_c.

With the recommended value, $k_{c_0} = 0.0096$ N/mm, obtained using Eq. (17), the force time history presents some low-frequency oscillations during the exit stage, starting when the force reaches its minimum value. Increasing the value of k_c reduces these oscillations and the amplitude of the negative peak force. For $k_c \geq 4 \times k_{c_0}$, the force signal does not oscillate anymore, but the negative peak force value is lower than for higher values of k_c. Convergence of the numerical results if achieved for $k_c \geq 8 \times k_{c_0}$. The amplitude of the positive peak force is less influenced by the value of k_c than the amplitude of the negative peak force. The cone results presented in Section 4 have been obtained with a value of $k_c = 16 \times k_{c_0} = 0.1536$ N/mm.

A similar convergence study has been carried out for the hemisphere case. The convergence of the results has been obtained for $k_c = 160 \times k_{c_0} = 1.536$ N/mm. This higher stiffness value is explained by the difference in geometry. Indeed, the flat bottom of the hemisphere leads to a more rapid increase of the hydrodynamic force during the first instants of the impact, requiring a higher contact stiffness for the numerical modelling. The hemisphere results presented in Section 4 have been obtained with a value of $k_c = 1.536$ N/mm.

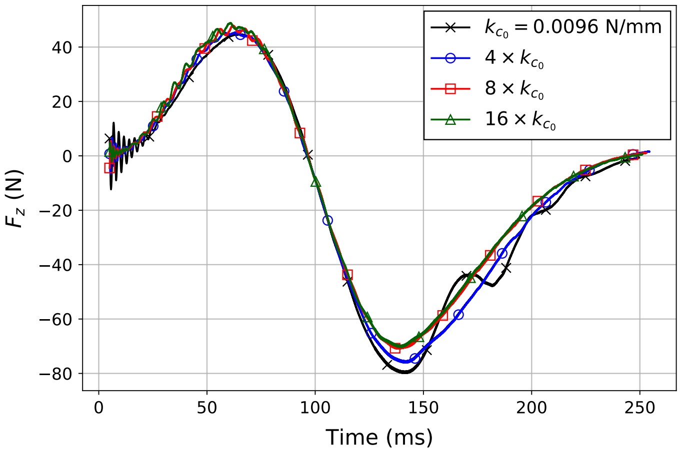

Figure 11: Time history of the hydrodynamic force during the water entry and subsequent exit of the cone, with $c_{max} = 250$ mm and $U_{max} = 0.6$ m/s. Different contact stiffness are tested. The contact stiffness $k_{c_0} = 0.0096$ N/mm is obtained when using Eq. (17).

3.3. Effect of the size of the fluid elements in the impact zone

In this section, the influence of the size of the fluid elements on the numerical results is investigated. Note that, as the present numerical model uses an explicit solver, the stable time-step of the computation also depends on the size of the fluid elements (via the CFL condition). The water entry and subsequent exit of the cone, with $c_{max} = 250$ mm and $U_{max} = 0.6$ m/s, is simulated using different sizes of fluid elements in the impact zone, $l_f = \{2; 2.5; 3; 4; 5; 7.5\}$ mm. To study the influence of the size of the fluid elements on the numerical results, in this section only, the vertical position of the structure is defined by Eq (1). The cone velocity is equal to 0.6 m/s until it reaches the level $z = \delta_z$. The contact stiffness is set to $k_c = 0.1536$ N/mm for all the fluid element sizes considered here. The results in terms of hydrodynamic forces are presented in Fig. 12.

The computation times corresponding to each numerical simulation are provided in Table 5. The computational time is larger when the fluid elements are smaller. Indeed, the number of fluid elements is higher, and the stable time step is smaller (higher number of time steps to reach the same physical time).

From Fig. 12, it is observed that the duration of the stages where the force is positive and negative is independent of the size of the fluid elements. However, the maximum and minimum values of the hydrodynamic force obtained numerically decrease with l_f. Indeed, the contact height h_c is proportional to l_f. Therefore, fewer fluid nodes interact with the structure, at a given time, for a lower value of l_f. Note that, in terms of force amplitude, the exit phase is slightly more sensitive to the size of the fluid elements than the entry phase. Indeed, the maximum hydrodynamic force obtained for $l_f \leq 3$ mm are similar (difference lower or equal to 1.6 N). A more pronounced difference is observed for the minimum hydrodynamic force obtained for $l_f \leq 3$ mm (difference lower or equal to 3.1 N).

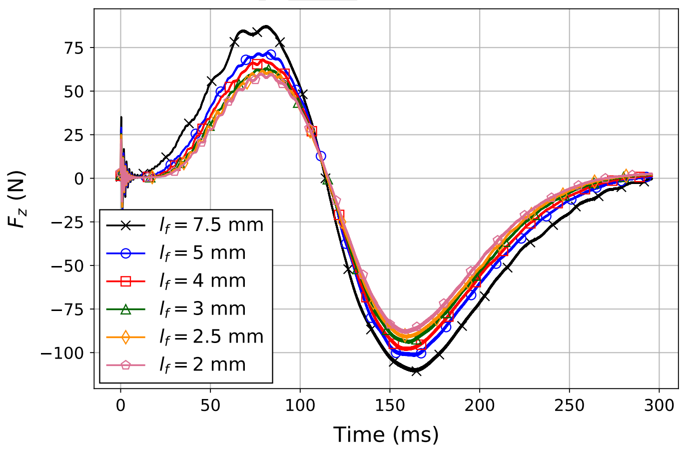

Figure 12: Time history of the hydrodynamic force during the water entry and subsequent exit of the cone, with $c_{max} = 250$ mm and $U_{max} = 0.6$ m/s. The considered sizes of the fluid elements in the impact zone are $l_f = \{2; 2.5; 3; 4; 5; 7.5\}$ mm.

l_f (mm)	7.5	5	4	3	2.5	2
Total number of fluid finite elements	526 176	1 376 160	2 397 008	5 102 208	8 140 520	14 682 662
Computation time (DD-hh:mm:ss)	04:19:34	19:05:12	1-01:03:24	2-10:34:12	3-11:02:05	12-02:31:53

Table 5: Simulation of the water entry and subsequent exit of the cone, with $c_{max} = 250$ mm and $U_{max} = 0.6$ m/s, for $l_f = \{2; 2.5; 3; 4; 5; 7.5\}$ mm. Comparison of the computation time and number of fluid finite elements associated with each model. 64 CPUs were used for all computations.

To further assess the convergence of the hydrodynamic force as a function of the size of the fluid elements, the Grid Convergence method (based on the Richardson extrapolation method [38]) has been applied to the present results. This method allows estimating (i) the continuum value (at zero grid spacing) of a quantity of interest from a series of lower-order discrete values and (ii) the error associated with the size of the grid used to discretize the simulation domain. The reader is referred to [39] for details and guidelines about the method. As explained in [40], this kind of error estimation method is sensitive to noise. A polynomial fit has been used on the numerical results to compensate for this limitation around the positive hydrodynamic force peak, where the oscillations are the strongest. The data used for this convergence study and the associated results are synthesized in Table 6. The maximum force values in Table 6 are obtained with the data fit.

	$\Phi = F_{z\ max}$	$\Phi = F_{z\ min}$
l_f (mm)	2, 2.5, 3	2, 2.5, 3
Φ_1	58.75 N	−88.69 N
Φ_2	60.57 N	−91.27 N
Φ_3	62.41 N	−94.36 N
p	1.05	1.91
Φ_{21}^{extr}	51.85 N	−83.83 N
e_1^a	13.30%	5.8%
e_2^a	16.8%	8.88%
e_3^a	20.36%	12.57%
GCI_{21}	14.68%	6.85%

Table 6: Data used to perform the convergence study based on the Grid Convergence method and associated results.

The application of the Grid Convergence method yields an order of convergence of $p = 1.05$ for $F_{z\ max}$ and $p = 1.91$ for $F_{z\ min}$. The estimated continuum values of the maximum and minimum hydrodynamic forces, together with the results obtained with different grid spacing, are presented in Fig. 13a and Fig. 13b, respectively. The maximum hydrodynamic force is extrapolated to be $F_{z\ max\ 21}^{extr} = 51.85$ N. The lower-scripts refer to the grid number (1 for $l_f = 2$ mm, 2 for $l_f = 2.5$ mm and 3 for $l_f = 3$ mm). The numerical uncertainty associated with the model $l_f = 2$ mm, regarding the extrapolated value, is $GCI_{21} = 14.68\%$ (Grid Convergence Index). The minimum hydrodynamic force is extrapolated to be $F^{extr}_{z\ min\ 21} = -83.83$ N, , with a GCI_{21} of 6.85%. The extrapolated relative error is the error between a value obtained for a given grid and the extrapolated continuous solution. This error is given by $e^a_n = \left| \frac{\Phi^{extr}_{21} - \Phi_{\ n}}{\Phi^{extr}_{21}} \right|$, with n the grid number. The extrapolated relative error obtained for the different grid spacing is presented in Fig. 14. Note that for a normalized grid spacing $r \leq 1.25$, *i.e.* for a fluid element size $l_f \leq 2.5$ mm, the extrapolated relative error remains under 16.8% for $F_{z\ max}$ and under 8.88% for $F_{z\ min}$.

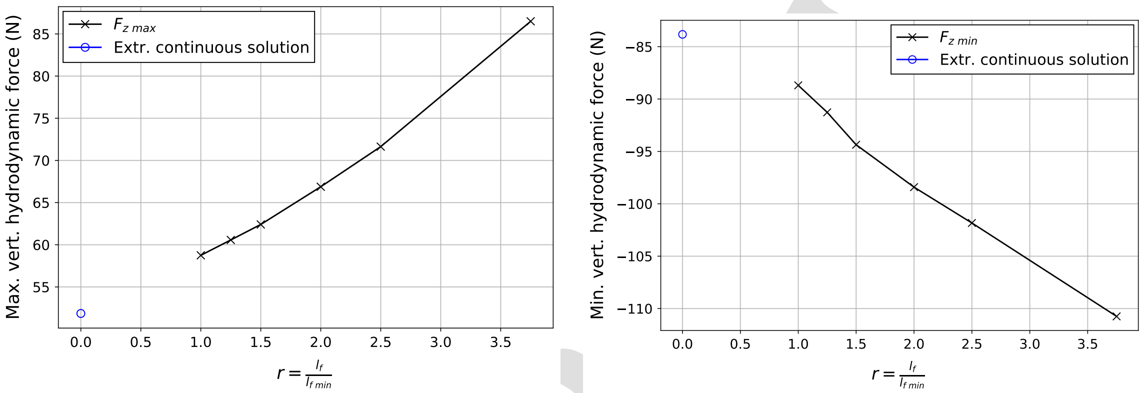

(a) (b)

Figure 13: Extrapolation of the (a) maximum and (b) minimum hydrodynamic force using the Richardson extrapolation method.

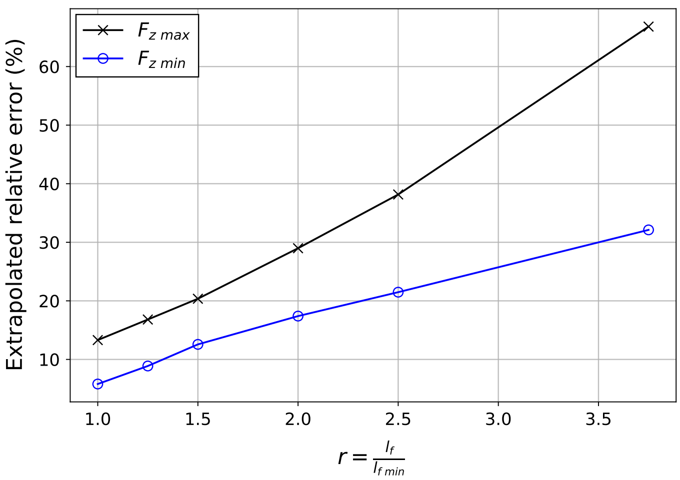

Figure 14: Estimation of the extrapolated relative error for the maximum and minimum hydrodynamic force associated for different normalized grid spacing.

In conclusion, the water entry and subsequent exit problem has been modelled using different fluid element sizes. The convergence of the numerical results has been estimated visually and with an error indicator based on an extrapolation method. It has been observed that for the considered sizes, (i) smaller fluid elements lead to more accurate numerical results and higher computation times, and (ii) the numerical results are not entirely converged. However, to maintain a reasonable computation time (with the model containing several millions of 3D fluid elements and the 64 CPUs used for the computation), it has been decided to set $l_f = 2.5$ mm for the investigations presented in the following sections. The loss of accuracy in terms of hydrodynamic force peak predictions, in comparison with the case $l_f = 2$ mm and with the extrapolated continuous solution, has been considered reasonable compared to the gain in computation time.

4. Comparisons with experimental results

In this section, the numerical results are compared to experimental data from [31] for the water entry and subsequent exit of a cone (Section 4.1) and a hemisphere (Section 4.2). The evolution of the non-dimensional hydrodynamic forces and the wetted surface radius are considered for several maximum impact velocities ($U_{max} \in [0.6; 0.4]$ m/s) and maximum wetted surface radius ($c_{max} \in [200; 250]$ mm). The evolution of the pressure coefficient at the different gauges locations (see Fig. 9) is given for the cone case, with $c_{max} = 250$ mm and $U_{max} = 0.6$ m/s, and for the hemisphere case, with $c_{max} = 200$ mm and $U_{max} = 0.4$ m/s.

The conclusions drawn from Section 3 are considered to define the numerical models, namely a water sound celerity $c_s = 500$ m/s and a mesh size $l_f = 2.5$ mm have been adopted. For the cone, the contact stiffness is set to $k_c = 0.1536$ N/mm. For the hemisphere, the contact stiffness is set to $k_c = 1.536$ N/mm.

4.1. Water entry and subsequent exit of a cone

In Fig. 15, the evolution of the hydrodynamic force is presented together with the position of the lowest point of the cone (h) and the cone velocity ($\dot{h}$) for the water entry and subsequent exit of a cone for $c_{max} = 250$ mm and $U_{max} = 0.6$ m/s.

After the first contact between the cone (or influence zone) and the water, the hydrodynamic force rapidly increases and reaches a maximum (positive force peak). Then, the force decreases and becomes negative (suction force) as the cone decelerates (see Fig. 15). As outlined in [31], when the force is null the cone velocity is still directed downward (along $-\vec{z}$). The force reaches its minimum at the transition between the entry and exit stages, *i.e.* when the cone velocity changes sign. Finally, the force gradually tends to zero.

The evolution of the non-dimensional hydrodynamic force during the water entry and subsequent exit of a cone is presented in Fig. 16a and 16b for $c_{max} = 250$ mm and $c_{max} = 200$ mm, respectively. The non-dimensional force is expressed depending on the non-dimensional time $t^* = \frac{U_{max} t}{R}$. Overall, the numerical model predicts with a rather good accuracy the evolution of the hydrodynamic force, for two different initial velocities and maximum penetration depths. In particular, the times at which the force reaches its maximum, its minimum and changes sign are well reproduced by the simulations. Notice that the stage during which the force is negative is longer than the one during which it is positive. However, the numerical model slightly underestimates the magnitude of the force peaks. These results may be related to the observations made in Section 3.3. Larger force peak magnitudes will likely be achieved with a finer mesh. Indeed, a finer mesh implies a smaller contact height (see Eq. (16)) and, thus, a cone kinematics closer to the experiments (*i.e.* a greater maximum penetration depth in the numerical model). The difference between experiments and simulations is more pronounced for the case $c_{max} = 200$ mm and $U_{max} = 0.57$ m/s, with $\Delta f_{adim\ max} = 11\%$ and $\Delta f_{adim\ min} = 5\%$ (see Fig. 16b). It is less perceptible for the lower impact velocity $U_{max} = 0.4$ m/s ($\Delta f_{adim\ max} = 3\%$ and $\Delta f_{adim\ min} = 9\%$) because of the oscillations of the experimental data.

During the entry stage, the evolution of the hydrodynamic force is independent of the velocity of the structure. The results diverge starting from the transition between the entry and exit stages, around $t^* = 0.25$ and $t^* = 0.18$ in Fig. 16a and Fig. 16b respectively. This divergence highlights the effect of the structure velocity, hence of gravity, on the evolution of the hydrodynamic force during the exit stage, as commented in [15]. For both experimental and numerical results, the effect of gravity is more pronounced for the lower values of U_{max}.

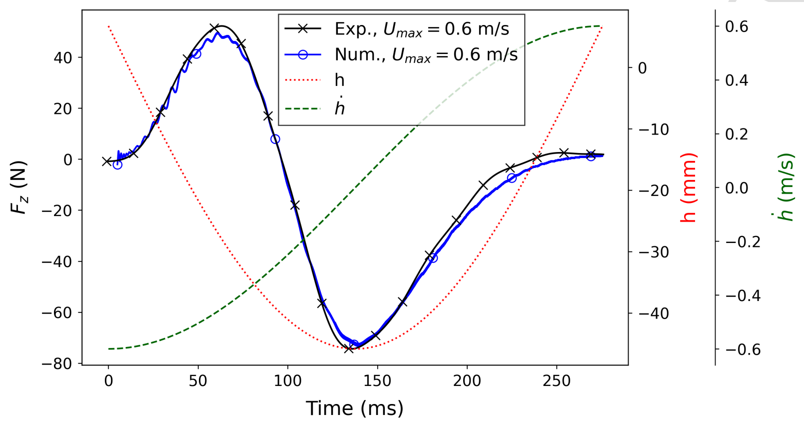

Figure 15: Time history of the hydrodynamic force, position of the lowest point of the cone (h) and the cone vertical velocity ($\dot{h}$) during the water entry and subsequent exit of a cone with $c_{max} = 250$ mm and $U_{max} = 0.6$ m/s.

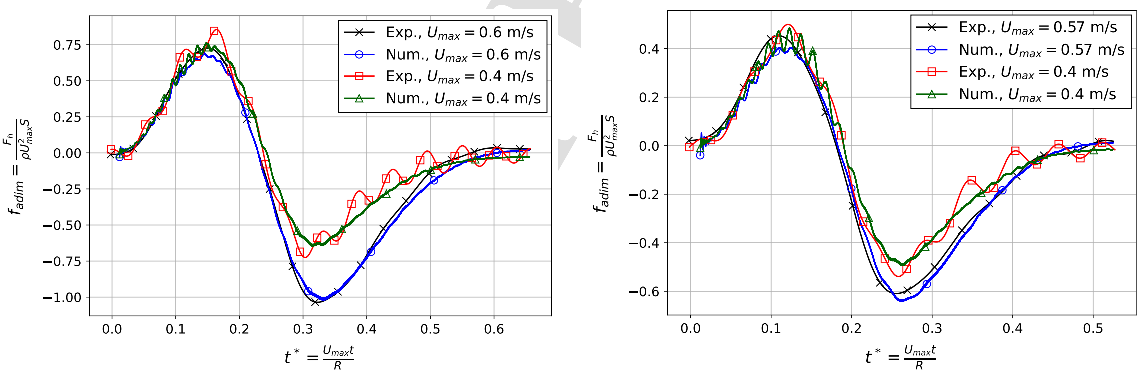

(a) (b)

Figure 16: Evolution of the non-dimensional hydrodynamic force depending on the non-dimensional time during the water entry and subsequent exit of the cone, with (a) $c_{max} = 250$ mm and $U_{max} = \{0.4; 0.6\}$ m/s and (b) $c_{max} = 200$ mm and $U_{max} = \{0.4; 0.57\}$ m/s.

The evolution of the pressure coefficient measured at the gauges $p1$-$p5$ during the water entry-exit of the cone ($c_{max} = 250$ mm and $U_{max} = 0.6$ m/s) is presented in Fig 17. This configuration features the maximum suction force amplitude of the configurations considered in this study. Positive pressure peaks are observed for the gauges $p1$ to $p4$ at the beginning of the entry stage ($t^* \leq 0.24$). The amplitude of the positive pressure peaks decreases as the cone decelerates: $p_{adim\ max\ p2} > p_{adim\ max\ p3} > p_{adim\ max\ p4}$. The relative pressure changes sign as the cone decelerates, around $t^* \simeq 0.24$, similarly to the instant when the hydrodynamic force changes sign (see Fig. 16a). The minimum relative pressures are measured around $t^* \simeq 0.33$. The minimum relative pressure are comprised between $p_{adim} = -0.63$ for $p5$ and $p_{adim} = -1.47$ for $p3$. Finally, the pressure returns toward $p_{adim} = 0$ at the end of the exit stage. One can note that the gauge $p5$ does not measure a positive pressure peak during the simulation. For this configuration, the occurrence of the minimum relative pressures corresponds to the occurrence of the minimum hydrodynamic force observed in Fig. 16a. It is however impossible to conclude about the accuracy of these pressure evolutions, as no corresponding experimental data is available.

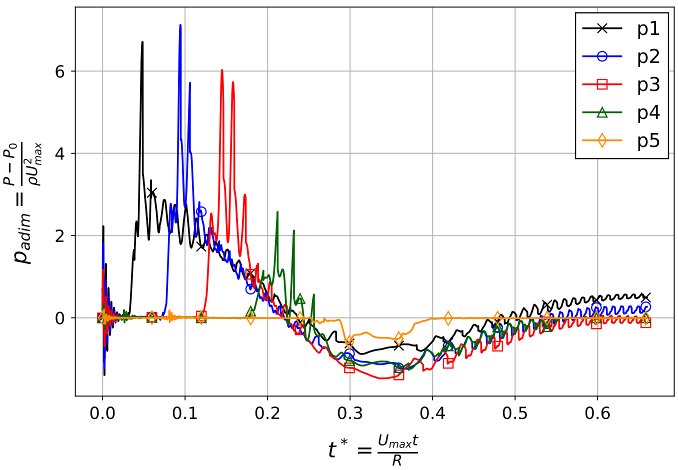

Figure 17: Evolution of the pressure coefficient at the gauges p1-p5 during the water entry and subsequent exit of the cone, with $c_{max} = 250$ mm and $U_{max} = 0.6$ m/s.

The evolution of the wetted surface radius for the water entry and subsequent exit of the cone is presented in Fig. 18a and 18b, for $c_{max} = 250$ mm and $c_{max} = 200$ mm, respectively. The numerical results stop before the experimental ones because the duration of the numerical simulations is inferior to the duration of the experiments, but note that the hydrodynamic force is already almost equal to zero at this stage (compare Fig. 16 and 18). For the considered body geometries and kinematics, the maximum wetted surface radius is attained when the penetration depth of the structure is maximum, i.e. when the cone velocity changes sign.

Overall, the numerical model accurately predicts the evolution of the wetted surface radius. However, it slightly underestimates the maximum value of the wetted surface radius. This is probably due to the absence of the water jets generated during the impact in the simulation. Indeed, the size of the fluid elements near the structure remains too large to model these thin jets. The numerical model also predicts a milder decrease of the wetted surface radius towards the end of the simulation.

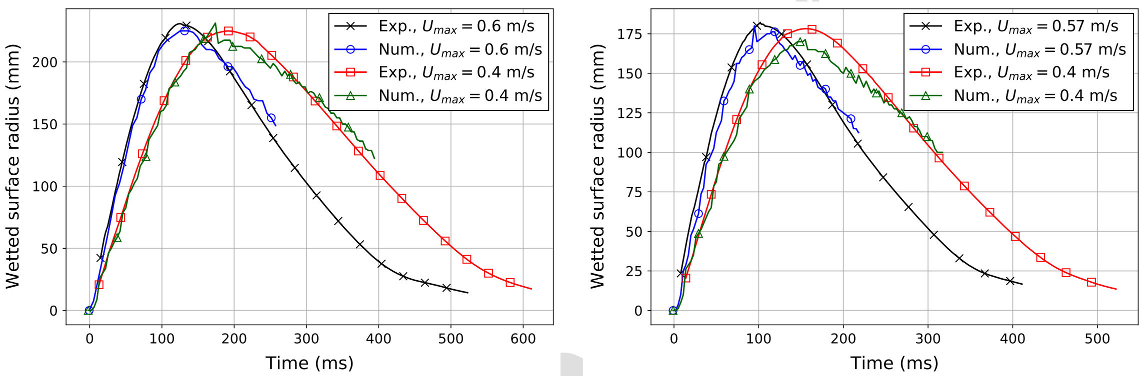

(a) (b)

Figure 18: Time history of the wetted surface radius during the water entry and subsequent exit of the cone, with (a) $c_{max} = 250$ mm and $U_{max} = \{0.4; 0.6\}$ m/s and (b) $c_{max} = 200$ mm and $U_{max} = \{0.4; 0.57\}$ m/s.

4.2. Water entry and subsequent exit of a hemisphere

The evolution of the non-dimensional hydrodynamic force during the water entry and subsequent exit of a hemisphere is presented in Fig. 19a and 19b, for $c_{max} = 250$ mm and $c_{max} = 200$ mm, respectively. The non-dimensional force is expressed depending on the non-dimensional time $t^* = \frac{U_{max} t}{R}$.

Contrary to the cone case, the non-dimensional hydrodynamic force is higher during the entry stage than during the exit stage. Otherwise, the observations are similar to those made for the cone. The numerical model accurately predicts the evolution of the hydrodynamic force. The case $c_{max} = 200$ mm and $U_{max} = 0.4$ m/s aside, $\Delta f_{adim\ max/min} \leq 5\%$. For the case $c_{max} = 200$ mm and $U_{max} = 0.4$ m/s, the difference between the experimental and numerical minimum force amplitudes is particularly high due to the oscillations of the experimental measures ($\Delta f_{adim\ min} \simeq 19\%$, see Fig. 19b). The effect of gravity on the evolution of the hydrodynamic force is also similar for the hemisphere. During the entry stage, the hydrodynamic force evolution is independent of the velocity of the structure. The results start diverging at the transition between the entry and exit stages, around $t^* = 0.15$ in Fig. 19b. Finally, the effect of gravity is more pronounced for the lower values of U_{max}.

In addition, a couple of observations can be made for the case $c_{max} = 250$ mm and $U_{max} = 0.6$ m/s. Firstly, a temporal discrepancy occurs at the end of the entry stage: the negative non-dimensional force peak occurs later in the simulation (see Fig. 19a). This temporal discrepancy is also visible for the case $c_{max} = 200$ mm and $U_{max} = 0.56$ m/s (see Fig. 19b). Secondly, the force measured experimentally at the end of the exit stage becomes positive before decreasing toward zero. Note that this phenomenon has also been observed numerically for the water entry and exit of an expanding and contracting circular cylinder (see Section 4.3., Fig. 8.c and 8.d, in reference [9]). The present numerical model predicts a different tendency: a gradual increase of the hydrodynamic force toward 0 N at the end of the exit stage. The reasons for this difference are unknown.

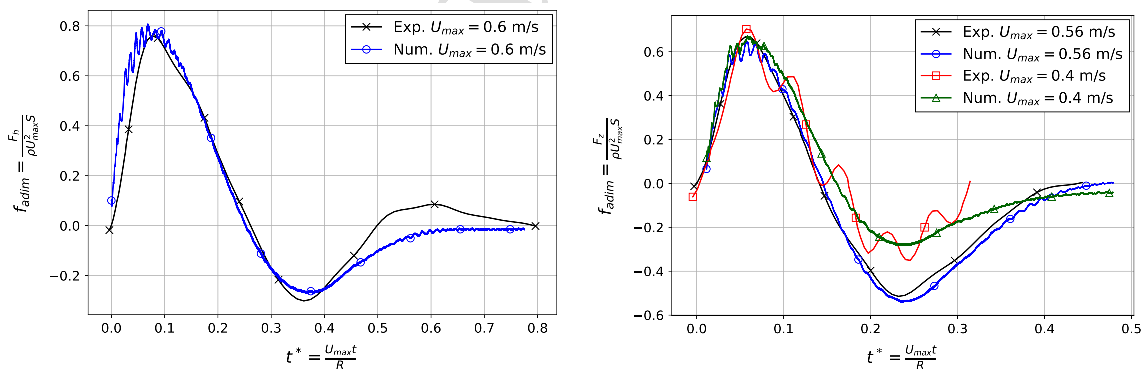

(a) (b)

Figure 19: Evolution of the non-dimensional hydrodynamic force depending on the non-dimensional time during the water entry and subsequent exit of the hemisphere, with (a) $c_{max} = 250$ mm and $U_{max} = 0.6$ m/s and (b) $c_{max} = 250$ mm and $U_{max} = \{0.4; 0.56\}$ m/s.

The evolution of the pressure coefficient, measured at the gauges $p1$ to $p5$ during the water entry-exit of the hemisphere ($c_{max} = 200$ mm and $U_{max} = 0.4$ m/s) is presented in Fig 20. This configuration features the minimum suction force amplitude of the configurations considered in this study. Positive pressure peaks are observed for the gauges $p1$ to $p3$ at the beginning of the entry stage ($t^* \leq 0.2$). The amplitude of the positive pressure peaks decreases as the hemisphere decelerates: $p_{adim\ max\ p2} > p_{adim\ max\ p3}$. A slightly negative relative pressure is observed for the gauges $p2$ and $p3$ starting from $t^* \simeq 0.22$. After the positive pressure peak, aside from the gauges $p2$ and $p3$, the relative pressure decreases toward $p_{adim} = 0$ at the end of the exit stage and remains positive. These results seem consistent with the low value of the suction force observed in Fig. 20. Again, it is impossible to conclude about the accuracy of these pressure evolutions, as no corresponding experimental data is available.

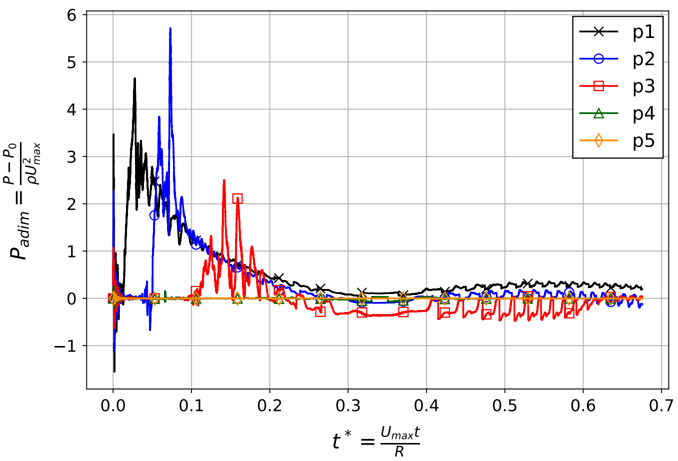

Figure 20: Evolution of the pressure coefficient at the gauges p1-p5 during the water entry and subsequent exit of the hemisphere, with $c_{max} = 200$ mm and $U_{max} = 0.4$ m/s.

The evolution of the wetted surface radius for the water entry and subsequent exit of the hemisphere had not been measured experimentally, as explained in [31]. Therefore, the corresponding numerical results are not presented.

5. Discussion and conclusion

In the present work, simulations of the water entry and subsequent exit of a cone and hemisphere have been analysed. Particular attention has been dedicated to the suction force prediction and the wetted surface evolution. As explained in the introduction, suction forces play an important role during aircraft ditching. The objective of the present study has been to assess the capacity of the presented numerical method to model suction forces. The computations have been carried out using a CEL approach and the explicit solver *Radioss*, developed by Altair. This numerical method is adapted to address both simple and more complex three-dimensional hydrodynamic impact problems. Comparisons have been made with existing experimental results. Overall, the numerical results are in good agreement with the experimental results. In particular, the numerical model predicts quite well the evolution of the hydrodynamic force and the transition from positive to negative (suction) force observed in the experiments (ranging from 60 N to -75 N). The fluid-structure interaction method is not able to model the thin jet generated during the impact, as observed in the experiments. Indeed, the size of the fluid elements near the structure is too large compared to the thickness of the jets. This may explain the slight underestimation of the wetted surface radius by the numerical model. Nonetheless, the evolution of the wetted surface is overall satisfactorily predicted. The sensitivity of the numerical results to different numerical parameters has been studied, especially to the contact stiffness and the size of the fluid elements in the impact zone (near the structure). The uncertainty associated with the results obtained for different sizes of fluid elements has been estimated using an extrapolation method. It appeared that the convergence of the numerical results could be attained with a finer spatial discretization of the fluid domain. However, a finer spatial discretization would drastically increase the computational cost as the model is 3D and features several millions of fluid elements. Therefore, an intermediary size of fluid elements has been selected as a compromise between precision and computational cost.

The evolution of the local pressure has been presented for two of the studied configurations: the cone case, with $c_{max} = 250$ mm and $U_{max} = 0.6$ mm; and the hemisphere case, with $c_{max} = 200$ mm and $U_{max} = 0.4$ mm. The cone and hemisphere cases respectively feature the maximum and minimum suction force amplitudes of the configurations considered in this study. These results show that the present method is able to provide insight into local pressure variations (near the structure) during water entry and subsequent exit problems. A negative relative pressure is observed for the cone case, and almost no negative relative pressure is observed for the hemisphere. Unfortunately, the experimental results do not include pressure measurements. Therefore, it is not possible to conclude about the accuracy of these pressure evolutions. However, as hydrodynamic impacts feature high spatial and temporal pressure gradients, it is supposed that a finer spatial discretization of the fluid domain would improve the precision of the computed pressure. The use of smaller fluid elements would obviously induce higher computation times.

This numerical method, validated for water entry and subsequent exit experiments led in a laboratory, could be applied to water impact simulations in realistic ditching conditions. Notice that the vertical velocity order of magnitude in the present cases is similar to the vertical velocity order of magnitude of an aircraft during ditching (less than 5 m/s). For instance, in [17], the ditching of a generic rigid aircraft body has been modelled with a structural vertical velocity of 1.5 m/s. Moreover, the same numerical method has been proved efficient to model high-velocity hydrodynamic impacts [35].

Future work will be dedicated to performing simulations and new experiments for more complex hydrodynamic impacts, more representative of realistic ditching conditions, involving a horizontal velocity and a wavy free surface. Also, the cavitation phenomenon could be considered in the present numerical method. Indeed, it is possible to take into account a cut-off pressure corresponding to the physical water vapour pressure (at a given temperature) in the water equation of state. Cavitation acts like a natural limit for the suction forces as it limits the magnitude of negative (relative) pressure in the water. Therefore, considering cavitation would be interesting when modelling hydrodynamic impacts with higher impact velocities, such as aircraft ditching [41].

Acknowledgement

The authors would like to thank ONERA (French aerospace research centre) and IFREMER (*Institut Français de Recherche pour l'Exploitation de la Mer*) for co-funding this project. The authors would like to thank Mathis LOVERINI (Altair) and Thierry SCHWOERTZIG (Altair) for the discussions that improved the quality of the results presented in this paper.

Declaration of interests

The authors report no conflict of interest.

References

[1] S. Abrate, Hull Slamming, Applied Mechanics Reviews 64 (2011) 1003. doi:10.1115/1.4023571.

[2] C. M. Seddon, M. Moatamedi, Review of water entry with applications to aerospace structures, International Journal of Impact Engineering 32 (7) (2006) 1045–1067. doi:10.1016/j.ijimpeng.2004.09.002.
URL https://www.sciencedirect.com/science/article/pii/S0734743X04001976

[3] T. von Karman, The Impact on Seaplane Floats During Landing, Report 321, NACA, Aerodynamical Institute of the Technical High School, Aachen, number: NACA-TN-321 (Oct. 1929).
URL https://digital.library.unt.edu/ark:/67531/metadc54062/

[4] H. Wagner, Phenomena Associated with Impacts and Sliding on Liquid Surfaces, Tech. rep., Translation of Über Stoß- und Gleitvorgänge an der Oberfläche von Flüssigkeiten. Z. Angew. Math. Mech. 12, 193–215 (in German) (1932).
URL http://archive.org/details/nasa_techdoc_20010003513

[5] H. Ribet, P. Laborde, M. Mahé, Numerical modeling of the impact on water of a flexible structure by explicit finite element method — Comparisons with Radioss numerical results and experiments, Aerospace Science and Technology 3 (2) (1999) 83–91. doi:10.1016/S1270-9638(99)80032-7.

URL https://www.sciencedirect.com/science/article/pii/S1270963899800327

[6] V. Faucher, M. Bulik, P. Galon, Updated VOFIRE algorithm for fast fluid–structure transient dynamics with multi-component stiffened gas flows implementing anti-dissipation on unstructured grids, Journal of Fluids and Structures 74 (2017) 64–89. doi:10.1016/j.jfluidstructs.2017.07.001.
URL https://www.sciencedirect.com/science/article/pii/S0889974616304960

[7] E. E. McBride, L. J. Fisher, Experimental investigation of the effect of rear-fuselage shape on ditching behavior, Report 2929, NACA, Langley Aeronautical Laboratory, Langley Field, Virginia, USA, number: NACA-TN-2929 (Apr. 1953).
URL https://digital.library.unt.edu/ark:/67531/metadc56694/m1/1/

[8] D. J. Piro, K. J. Maki, Hydroelastic analysis of bodies that enter and exit water, Journal of Fluids and Structures 37 (2013) 134–150. doi:10.1016/j.jfluidstructs.2012.09.006.
URL http://www.sciencedirect.com/science/article/pii/S0889974612001806

[9] A. Tassin, D. J. Piro, A. A. Korobkin, K. J. Maki, M. J. Cooker, Two-dimensional water entry and exit of a body whose shape varies in time, Journal of Fluids and Structures 40 (2013) 317–336. doi:10.1016/j.jfluidstructs.2013.05.002.
URL http://www.sciencedirect.com/science/article/pii/S0889974613001187

[10] K. Hughes, R. Vignjevic, J. Campbell, T. De Vuyst, N. Djordjevic, L. Papagiannis, From aerospace to offshore: Bridging the numerical simulation gaps–Simulation advancements for fluid structure interaction problems, International Journal of Impact Engineering 61 (2013) 48–63. doi:10.1016/j.ijimpeng.2013.05.001.

URL https://www.sciencedirect.com/science/article/pii/S0734743X13001073

[11] C. E. Brennen, Cavitation and bubble dynamics, no. 44 in Oxford engineering science series, Oxford University Press, New York, 1995.

[12] C. Judge, A. Troesch, M. Perlin, Initial water impact of a wedge at vertical and oblique angles, Journal of Engineering Mathematics 48 (3) (2004) 279–303. doi:10.1023/B:engi.0000018187.33001.e1.
URL https://doi.org/10.1023/B:engi.0000018187.33001.e1

[13] D. H. Peregrine, L. Thais, The effect of entrained air in violent water wave impacts, Journal of Fluid Mechanics 325 (1996) 377–397. doi:10.1017/S0022112096008166.
URL https://www.cambridge.org/core/product/identifier/S0022112096008166/type/journal_article

[14] G. N. Bullock, A. R. Crawford, P. J. Hewson, M. J. A. Walkden, P. A. D. Bird, The influence of air and scale on wave impact pressures, Coastal Engineering 42 (4) (2001) 291–312. doi:10.1016/S0378-3839(00)00065-X.
URL https://www.sciencedirect.com/science/article/pii/S037838390000065X

[15] A. Del Buono, G. Bernardini, A. Tassin, A. Iafrati, Water entry and exit of 2D and axisymmetric bodies, Journal of Fluids and Structures 103 (2021) 103269. doi:10.1016/j.jfluidstructs.2021.103269.
URL https://www.sciencedirect.com/science/article/pii/S0889974621000529

[16] N. R. S. Toso, Contribution to the modelling and simulation of aircraft structures impacting on water, Ph.D. thesis, Institute of Aircraft Design, Universität

Stuttgart, accepted: 2009-12-18 (2009).
URL http://elib.uni-stuttgart.de/handle/11682/3840

[17] B. Langrand, M. H. Siemann, Full aircraft ditching simulation: a comparative analysis of advanced coupled fluid-structure computational methods, International Conference on Impact Loading of Structures and Materials (2018) 4.

[18] J. Donea, A. Huerta, J.-P. Ponthot, A. Rodríguez-Ferran, Encyclopedia of computational mechanics - Chapter 14, John Wiley, Chichester, West Sussex, 2004, oCLC: ocm55800932.

[19] L. B. Lucy, A numerical approach to the testing of the fission hypothesis, The Astronomical Journal 82 (1977) 1013–1024. doi:10.1086/112164.
URL http://adsabs.harvard.edu/abs/1977AJ.....82.1013L

[20] J. J. Monaghan, Simulating Free Surface Flows with SPH, Journal of Computational Physics 110 (2) (1994) 399–406. doi:10.1006/jcph.1994.1034.
URL https://www.sciencedirect.com/science/article/pii/S0021999184710345

[21] M. Souli, J.-F. Sigrist, Interaction fluide-structure: Modélisation et simulation numérique, Vol. 19, Hermès - Lavoisier, 2010.
URL https://www.tandfonline.com/doi/full/10.1080/17797179.2010.9737468

[22] F. Casadei, N. Leconte, M. Larcher, Strong and weak forms of a fully non-conforming FSI algorithm in fast transient dynamics for blast loading of structures, in: EU Science Hub - European Commission, Corfu, Greece, 2011, p. 20.
URL https://ec.europa.eu/jrc/en/publication/contributions-conferences/strong-and-weak-forms-fully-non-conforming-fsi-algorith

[23] I. Stenius, A. Rosén, J. Kuttenkeuler, Explicit FE-modelling of fluid–structure interaction in hull–water impacts, International Shipbuilding Progress 53 (2) (2006) 103–121, publisher: IOS Press.
URL https://content.iospress.com/articles/international-shipbuilding-progress/isp006

[24] I. Stenius, A. Rosén, J. Kuttenkeuler, Explicit FE-modelling of hydroelasticity in panel-water impacts, International Shipbuilding Progress 54 (2-3) (2007) 111–127, publisher: IOS Press.
URL https://content.iospress.com/articles/international-shipbuilding-progress/isp022

[25] I. Stenius, A. Rosén, J. Kuttenkeuler, Hydroelastic interaction in panel-water impacts of high-speed craft, Ocean Engineering 38 (2) (2011) 371–381. doi:10.1016/j.oceaneng.2010.11.010.
URL https://www.sciencedirect.com/science/article/pii/S0029801810002556

[26] M. H. Siemann, B. Langrand, Coupled fluid-structure computational methods for aircraft ditching simulations: Comparison of ALE-FE and SPH-FE approaches, Computers & Structures 188 (2017) 95–108. doi:10.1016/j.compstruc.2017.04.004.
URL http://www.sciencedirect.com/science/article/pii/S0045794916312998

[27] T. Xiao, N. Qin, Z. Lu, X. Sun, M. Tong, Z. Wang, Development of a smoothed particle hydrodynamics method and its application to aircraft ditching simulations, Aerospace Science and Technology 66 (2017) 28–43. doi:10.1016/j.ast.2017.02.022.
URL https://www.sciencedirect.com/science/article/pii/S1270963817303413

[28] C. Chen, A.-M. Zhang, J.-Q. Chen, Y.-M. Shen, SPH simulations of water entry problems using an improved boundary treatment, Ocean Engineering 238 (2021) 109679. doi:10.1016/j.oceaneng.2021.109679.
URL https://www.sciencedirect.com/science/article/pii/S0029801821010532

[29] M. Überrück, all WP2 contributing partners, D2.2: Progress Report, Tech. rep., Increased Safety & Robust Certification for ditching of Aircrafts & Helicopters (Sep. 2018).

[30] TUHH, , all WP2 contributing partners, D2.4: Final Report - Benchmarking, Tech. rep., Increased Safety & Robust Certification for ditching of Aircrafts & Helicopters (Feb. 2020).

[31] T. Breton, A. Tassin, N. Jacques, Experimental investigation of the water entry and/or exit of axisymmetric bodies, Journal of Fluid Mechanics 901, publisher: Cambridge University Press (Oct. 2020). doi:10.1017/jfm.2020.559.
URL https://www.cambridge.org/core/journals/journal-of-fluid-mechanics/article/experimental-investigation-of-the-water-entry-B9E3CA11EA4C3493F92ABBB9B3B04D01

[32] J. Gobeltz, P. Gythiel, Essai d'amerrissage forcé sur bassin d'une maquette au 1/16 ème de l'avion Mercure, Tech. Rep. 74-05, Institut de Mécanique des FLuides de Lille (IMFL), Lille, France (Feb. 1974).

[33] A. Tassin, T. Breton, B. Forest, J. Ohana, S. Chalony, D. Le Roux, A. Tancray, Visualization of the contact line during the water exit of flat plates, Experiments in Fluids 58 (8) (2017) 104. doi:10.1007/s00348-017-2383-1.
URL https://doi.org/10.1007/s00348-017-2383-1

[34] R. Saurel, F. Petitpas, R. A. Berry, Simple and efficient relaxation methods for interfaces separating compressible fluids, cavitating flows and shocks in

multiphase mixtures, Journal of Computational Physics 228 (5) (2009) 1678–1712. doi:10.1016/j.jcp.2008.11.002.
URL https://www.sciencedirect.com/science/article/pii/S0021999108005895

[35] M. Goron, B. Langrand, T. Fourest, N. Jacques, A. Tassin, Assesment of coupled lagrangian eulerian finite element simulations to model suction forces during hydrodynamic impacts, International Conference on High Performance and Optimum Structures and Materials Encompassing Shock and Impact Loading (2022) 12.

[36] D. Delsart, B. Langrand, A. Vagnot, Evaluation of a Euler/Lagrange coupling method for the ditching simulation of helicopter structures, in: WIT Transactions on the Built Environment, Vol. 105, Royal Mare Village, Crete, Greece, 2009. doi:10.2495/fsi090241.

[37] A. Bayliss, E. Turkel, Outflow Boundary Conditions for Fluid Dynamics, SIAM Journal on Scientific and Statistical Computing 3 (Jul. 1982). doi:10.1137/0903016.

[38] L. F. Richardson, J. A. Gaunt, VIII. The deferred approach to the limit, Philosophical Transactions of the Royal Society of London. Series A, Containing Papers of a Mathematical or Physical Character 226 (636-646) (1927) 299–361, publisher: Royal Society. doi:10.1098/rsta.1927.0008.
URL https://royalsocietypublishing.org/doi/abs/10.1098/rsta.1927.0008

[39] I. B. Celik, U. Ghia, P. J. Roache, C. J. Freitas, H. Coleman, P. E. Raad, Procedure for Estimation and Reporting of Uncertainty Due to Discretization in CFD Applications, Journal of Fluids Engineering 130 (7) (Jul. 2008). doi:10.1115/1.2960953.
URL https://doi.org/10.1115/1.2960953

[40] L. Eça, M. Hoekstra, A procedure for the estimation of the numerical uncertainty of CFD calculations based on grid refinement studies, Journal of Computational Physics 262 (2014) 104–130. doi:10.1016/j.jcp.2014.01.006.
URL https://www.sciencedirect.com/science/article/pii/S0021999114000278

[41] A. Iafrati, S. Grizzi, Cavitation and ventilation modalities during ditching, Physics of Fluids 31 (5) (2019) 052101, publisher: American Institute of Physics. doi:10.1063/1.5092559.
URL https://aip.scitation.org/doi/full/10.1063/1.5092559

The authors report no conflict of interest.